SCIENCE CHINA
Physics, Mechanics & Astronomy

Anisotropic magnetoelastic response in the magnetic Weyl semimetal Co$_3$Sn$_2$S$_2$

Chang Liu, ChangJiang Yi, XingYu Wang, JianLei Shen, Tao Xie, Lin Yang, Tom Fennel, Uwe Stuhr[3], ShiLiang Li[3], HongMing Weng[3], YouGuo Shi[3], EnKe Liu[3] and HuiQian Luo[3]

Citation: SCIENCE CHINA Physics, Mechanics & Astronomy **64**, 257511 (2021); doi: 10.1007/s11433-020-1655-2

View online: https://engine.scichina.com/doi/10.1007/s11433-020-1655-2

View Table of Contents: https://engine.scichina.com/publisher/scp/journal/SCPMA/64/5

Published by the Science China Press

SCIENCE CHINA
Physics, Mechanics & Astronomy

• Article •

May 2021 Vol. 64 No. 5: 257511
https://doi.org/10.1007/s11433-020-1655-2

Anisotropic magnetoelastic response in the magnetic Weyl semimetal $Co_3Sn_2S_2$

Chang Liu[1,2†], ChangJiang Yi[1,2†], XingYu Wang[1,2†], JianLei Shen[1,2], Tao Xie[1,2], Lin Yang[1,2], Tom Fennel[1,3], Uwe Stuhr[3], ShiLiang Li[1,2,4], HongMing Weng[1,2,4,5,6], YouGuo Shi[1,2,4,6*], EnKe Liu[1,4*], and HuiQian Luo[1,4*]

[1]*Beijing National Laboratory for Condensed Matter Physics, Institute of Physics, Chinese Academy of Sciences, Beijing 100190, China;*
[2]*School of Physical Sciences, University of Chinese Academy of Sciences, Beijing 100190, China;*
[3]*Laboratory for Neutron Scattering and Imaging, Paul Scherrer Institute, Villigen CH-5232, Switzerland;*
[4]*Songshan Lake Materials Laboratory, Dongguan 523808, China;*
[5]*CAS Centre for Excellence in Topological Quantum Computation, Beijing 100190, China;*
[6]*Physical Science Laboratory, Huairou National Comprehensive Science Center, Beijing 101400, China*

Received October 27, 2020; accepted December 24, 2020; published online February 8, 2021

$Co_3Sn_2S_2$ is a recently identified magnetic Weyl semimetal in Shandite compounds. Upon cooling, $Co_3Sn_2S_2$ undergoes a ferromagnetic transition with *c*-axis polarized moments (~0.3 μ_B/Co) around T_C = 175 K, followed by another magnetic anomaly around $T_A \approx 140$ K. A large intrinsic anomalous Hall effect is observed in the magnetic state below T_C with a maximum of anomalous Hall angle near T_A. Here, we report an elastic neutron scattering on the crystalline lattice of $Co_3Sn_2S_2$ in a magnetic field up to 10 T. A strongly anisotropic magnetoelastic response is observed, while only a slight enhancement of the Bragg peaks is observed when $\mathbf{B}//c$. The in-plane magnetic field ($\mathbf{B}//ab$) dramatically suppresses the Bragg peak intensity probably by tilting the moments and lattice toward the external field direction. The in-plane magnetoelastic response commences from T_C, and as it is further strengthened below T_A, it becomes nonmonotonic against the field between T_A and T_C because of the competition from another in-plane magnetic order. These results suggest that a magnetic field can be employed to tune the $Co_3Sn_2S_2$ lattice and its related topological states.

Weyl semimetal, magneto-elastic coupling, topological materials, elastic neutron scattering, ferromagnetism

PACS number(s): 71.55.Ak, 25.40.Dn, 61.12.-q, 75.30.-m, 75.50.Gg

Citation: C. Liu, C. J. Yi, X. Y. Wang, J. L. Shen, T. Xie, L. Yang, T. Fennel, U. Stuhr, S. L. Li, H. M. Weng, Y. G. Shi, E. K. Liu, and H. Q. Luo, Anisotropic magnetoelastic response in the magnetic Weyl semimetal $Co_3Sn_2S_2$, Sci. China-Phys. Mech. Astron. **64**, 257511 (2021), https://doi.org/10.1007/s11433-020-1655-2

1 Introduction

The magnetic Weyl semimetals (MWSMs) with broken time-reversal symmetry have been considered as one of the ideal hosts for achieving intrinsic anomalous Hall effect (AHE) [1-8]. In these materials, the Weyl nodes can be viewed as pairs of magnetic monopoles with opposite chirality in momentum space, and the wave packets from the Weyl fermions possess high anomalous velocity [6-9]. If they are sufficiently close to the Fermi energy (E_F), and the individual Fermi surface sheets possess nonzero Chern numbers, the Berry curva-

*Corresponding authors (YouGuo Shi, email: ygshi@iphy.ac.cn;
EnKe Liu, email: ekliu@iphy.ac.cn; HuiQian Luo, email: hqluo@iphy.ac.cn)
†These authors contributed equally to this work.

ture of occupied electronic Bloch states is thus significantly enhanced [10-12]. According to the Karplus-Luttinger mechanism [13], a large intrinsic AHE, where the anomalous Hall conductivity (AHC) is nearly proportional to the distance between a pair of the Weyl nodes and strongly coupled with the magnetic order [1, 3, 6], is expected owing to the presence of strong spin-orbit coupling (SOC).

Recently, a half-metallic ferromagnet, $Co_3Sn_2S_2$, was identified as MWSM, and it possessed high intrinsic AHC (1130 Ω^{-1} cm^{-1}) and a large anomalous Hall angle (20%) [14-16]. $Co_3Sn_2S_2$ has been known as a Co-based Shandite compound for many years [17, 18]. It has a rhombohedral structure (space group: $R\bar{3}m$) consisting of quasi-two-dimensional Co_3Sn and S_2Sn layers that are stacked in the ABC fashion along the c-axis where the magnetic Co atoms are arranged on a corner-sharing kagome lattice in the ab-plane (Figure 1(a)) [17-20]. The electronic bands near E_F are dominated by the 3d-orbitals of Co with only a spin-up channel for its half-metallic nature [21, 22], forming a ferromagnetic order below $T_C \approx 175$ K with a c-axis polarized magnetic moment of ~ 0.3 μ_B/Co [22-24]. The first-principle calculations utilizing SOC have predicted the linear band crossings and three pairs of Weyl nodes in the first Brillouin zone [14, 15, 25], which have been recently confirmed by angle-resolved photoemission spectroscopy and scanning tunneling spectroscopy experiments, for its topological Fermi arcs on the surface and the topological bands in the bulk with a nonzero Chern number ($n = +1$) [15, 26, 27]. Although the intrinsic AHE originates mainly from the Weyl fermions near E_F, the interplay between the Weyl fermions and Co moments is also essential for AHC [15,28,29], where it saturates far below T_C. However, the anomalous Hall resistivity ρ_H^A attains a maximum that is just below T_C [14, 15]. Notably, there is another magnetic anomaly below T_C that is designated as T_A (~ 140 K), which may be explained as the formation of a competing phase with a nontrivial spin texture like skyrmions or in-plane antiferromagnetic order [30,31]. However, T_A is sensitive to the strength and orientation of the external magnetic field, as well as the hydrostatic pressure [31]. Furthermore, it appears as the orbits contribute significantly to the magnetism far below T_A and T_C, thereby inducing an anomalous Zeeman effect with negative magnetism and locally bound spin-orbit polarons [32-34]. Our recent transport measurements also revealed a strong magnetocrystalline anisotropy with K_u of up to 8.3×10^5 J m^{-3} and out-of-plane angular dependent Hall conductivity in an external magnetic field [35]. Further, inelastic neutron scattering experiments have revealed an intimate interplay between the low-energy-spin dynamics and topological Weyl fermions [36-38]. All the above facts clearly indicate that the association of SOC with its complex magnetism is vital to the topological physical properties of the magnetic Weyl semimetal $Co_3Sn_2S_2$.

Here, we report an elastic neutron scattering study of a single crystal of $Co_3Sn_2S_2$ in a magnetic field B of up to 10 T. The magnetoelastic responses of **B**//c and **B**//ab (Figure 1(b)) were very different, while there was only a slight enhancement of the Bragg peaks in the field along the c-axis, the in-plane field dramatically suppressed the peak intensity by possibly aligning the moments and tilting the lattice toward

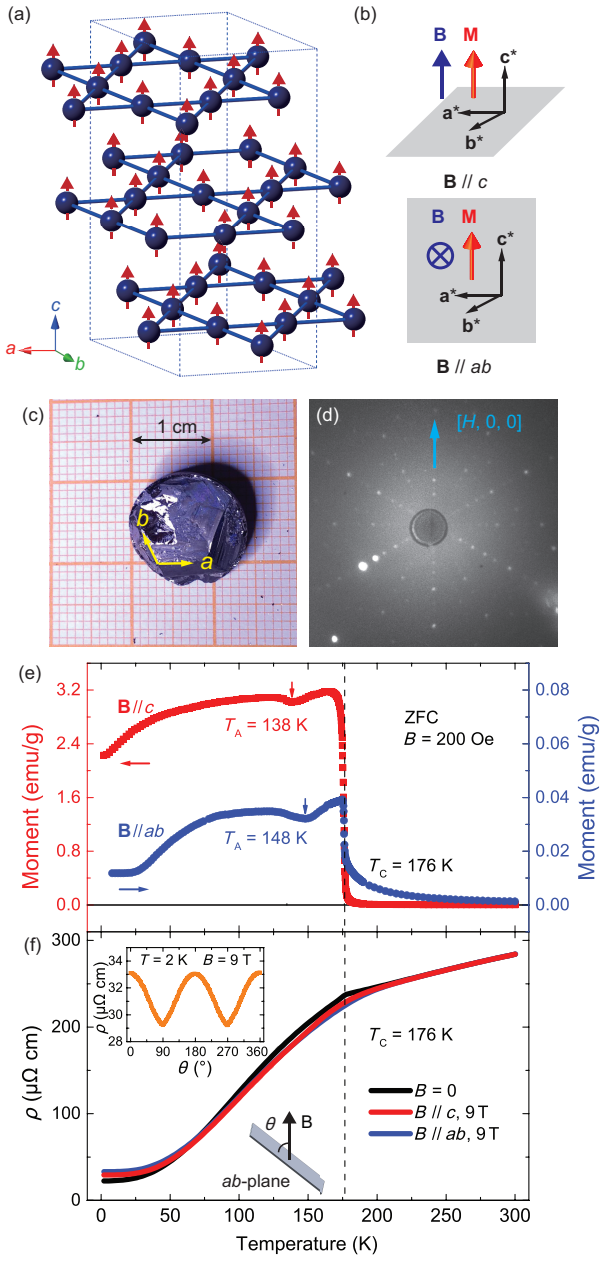

Figure 1 (Color online) (a) Ferromagnetic structure of the Co kagome lattice in the $Co_3Sn_2S_2$ compound. (b) Geometries of the magnetic field, effective moment, and reciprocal lattice. The neutron scattering plane is marked as a gray square. (c) Crystal sizes and crystalline orientation of the compound. (d) X-ray Laue reflection patterns of the crystal. (e) Magnetizations in the **B**//c (left axis) and **B**//ab-plane (right axis) cases. (f) Longitudinal in-plane resistivities for the $B = 0$ T, **B**//c, and **B**//ab cases at 9 T. The inset shows the anisotropy of the resistivity at $T = 2$ K and $B = 9$ T.

the field direction. The in-plane magnetoelastic response mostly occurred below T_A where only the out-of-plane ferromagnetic state exists. It exhibited a nonmonotonic behavior upon applying a magnetic field between T_A and T_C, and finally disappeared above T_C. Therefore, the magnetoelastic coupling in $Co_3Sn_2S_2$ was very strong but anisotropic, thus enabling it to tune its magnetism and lattice, as well as topological states in an external magnetic field.

2 Experiments

A centimeter-sized $Co_3Sn_2S_2$ single crystal was grown by the self-flux method, which was different from the Sn/Pb-flux method, as previously reported [14,19,20] (Figure 1(c)). The crystal possessed a hexagonal cleaved surface at the top and exhibited hexagonal symmetry of the X-ray Laue reflection pattern along the *ab*-plane, which accounted for its high quality (Figure 1(c) and (d)). This crystal weighed approximately 6.3 g and was cut into two nearly identical pieces for two different geometries in neutron scattering measurements, which were $\mathbf{B}//\mathbf{M}//\mathbf{c}^*$ ($\mathbf{B}//c$) and $\mathbf{B} \perp \mathbf{c}^*, \mathbf{a}^*$, namely $\mathbf{B}//ab$ or specifically, $\mathbf{B}//b$, respectively (Figure 1(b)). A clear ferromagnetic transition was observed at $T_C = 176$ K in the strongly anisotropic zero-field-cooling (ZFC) magnetization, followed by another magnetic anomaly at $T_A = 138$ K for $\mathbf{B}//c$ and $T_A = 148$ K (defined here as the dip of $M(T)$) for $\mathbf{B}//ab$, which is related to the formation of a nontrivial spin texture or an in-plane antiferromagnetic order (Figure 1(e)) [30,31]. Notably, T_A is possibly sample-dependent because of the different growth procedures, and it is also sensitive to the measured magnetic field strength and directions. The details of the magnetization below T_A are also sample-dependent, and T_C of the sample in this study is slightly higher than that of the sample that was grown by the Sn/Pb-flux method [36]. A slightly anisotropic response of the magnetic field was also observed below T_C in the in-plane resistivity (Figure 1(f)) with a four-fold rotation symmetry (inset of Figure 1(f)), while no trace of T_A was observed in all the resistivity measurements [35].

The elastic neutron scattering experiments were performed with thermal triple-axis spectrometers EIGER at SINQ (PSI, Switzerland) with fixed final energy, $E_f = 14.7$ meV, a highly oriented pyrolytic graphite monochromator, and an analyzer. A cryomagnet with a vertical field of up to 10 T and temperatures down to 2 K was utilized in our measurements. Each $Co_3Sn_2S_2$ crystal was stably mounted on a thick aluminum alloy plate by hydrogen-free glue and aluminum wires to ensure that the sample could not be pulled off by the magnetic torque. Each sample was placed at the center of the aluminum plate, near the fastened crew. Thus, the plate could not be easily bent by small magnetic torque. The scattering planes, $[H,0,0]\times[0,0,L]$ for $\mathbf{B}//ab$ and $[H,0,0]\times[0,K,0]$ for $\mathbf{B}//c$, were defined by the unit cell ($a = b = 5.35$ Å, $c = 13.10$ Å, $\alpha = \beta = 90°$, and $\gamma = 120°$. The vector, $\mathbf{Q}$, in the reciprocal space was defined as $\mathbf{Q} = H\mathbf{a}^* + K\mathbf{b}^* + L\mathbf{c}^*$, where H, K, and L are the Miller indices, and $\mathbf{a}^* = [(\sqrt{3}\hat{\mathbf{x}} + \hat{\mathbf{y}})/\sqrt{3}]\times(2\pi/a)$, $\mathbf{b}^* = (2\hat{\mathbf{y}}/\sqrt{3})\times(2\pi/a)$, $\mathbf{c}^* = \hat{\mathbf{z}}2\pi/c$ are the reciprocal lattice units. Thus, the d-spacing is expressed as follows: $d_{HKL} = 1/\sqrt{4(H^2+HK+K^2)/3a^2 + L^2/c^2}$. The sample mosaic, which is defined by FWHM of the rocking curve (θ-scan) was approximately 0.8° for the $Q = (3, 0, 0)$ peak (in-plane) and approximately 1° for the $Q = (0, 0, 3)$ peak (out-of-plane). The field dependence was measured employing the elastic Q-scans of the Bragg peaks with the field changing from 0 to 10 T (or 10 to 0 T) at a rate of 1 T per step. Here, the Q-scans were performed by either the H-scan along the $[H,0,0]$ direction or the L-scan along the $[0,0,L]$ direction. After several cycles of the field change, the result of each Bragg peak in the same environment was reversible in both the ZFC or field-cooling (FC) methods. For example, when the sample was first cooled down in the field $B = 10$ T to the ferromagnetic state, followed by a decrease of the field to zero, the Q-scan results were the same as those of the zero-field measurements. In principle, below T_C, additional ferromagnetic contributions were evident in almost all the nuclear peaks with different ratios of the magnetic form factor to the nuclear structural factor. In our experiment, Peak (1, 0, 1) obtained the highest ratio of ferromagnetic contribution below T_C.

3 Results

Firstly, we presented the magnetic field effect on the Bragg peaks at a base temperature, $T = 2$ K, as shown in Figure 2. For easy comparison, we normalized the intensities by applying the maximum (from 0 to 1) of each measured peak under zero field. The scan directions were also marked in each panel. In the geometry of $\mathbf{B}//c$, the scattering plane, $[H,0,0]\times[0,K,0]$, and the limited scattering angle of the spectrometer only allowed us to access two Bragg peaks at $Q = (1, 1, 0)$ and $(3, 0, 0)$. Upon applying a magnetic field from 0 to 10 T along the c-axis, the peak intensity and peak width did not exhibit evident changes in both Bragg peaks (Figure 2(a) and (b)).

Thereafter, we focused on another geometry with $\mathbf{B}//ab$ and the $[H,0,0]\times[0,0,L]$ scattering plane. Besides the in-plane peak at $Q = (3, 0, 0)$, we could access more peaks such as $Q = (0, 0, 3)$, $(0, 0, 6)$, and $(0, 0, 9)$, along the L-direction and other peaks, such as $Q = (1, 0, 1)$, $(2, 0, 2)$, and $(3, 0, 3)$. Among these peaks, the $Q = (1, 0, 1)$ one ex-

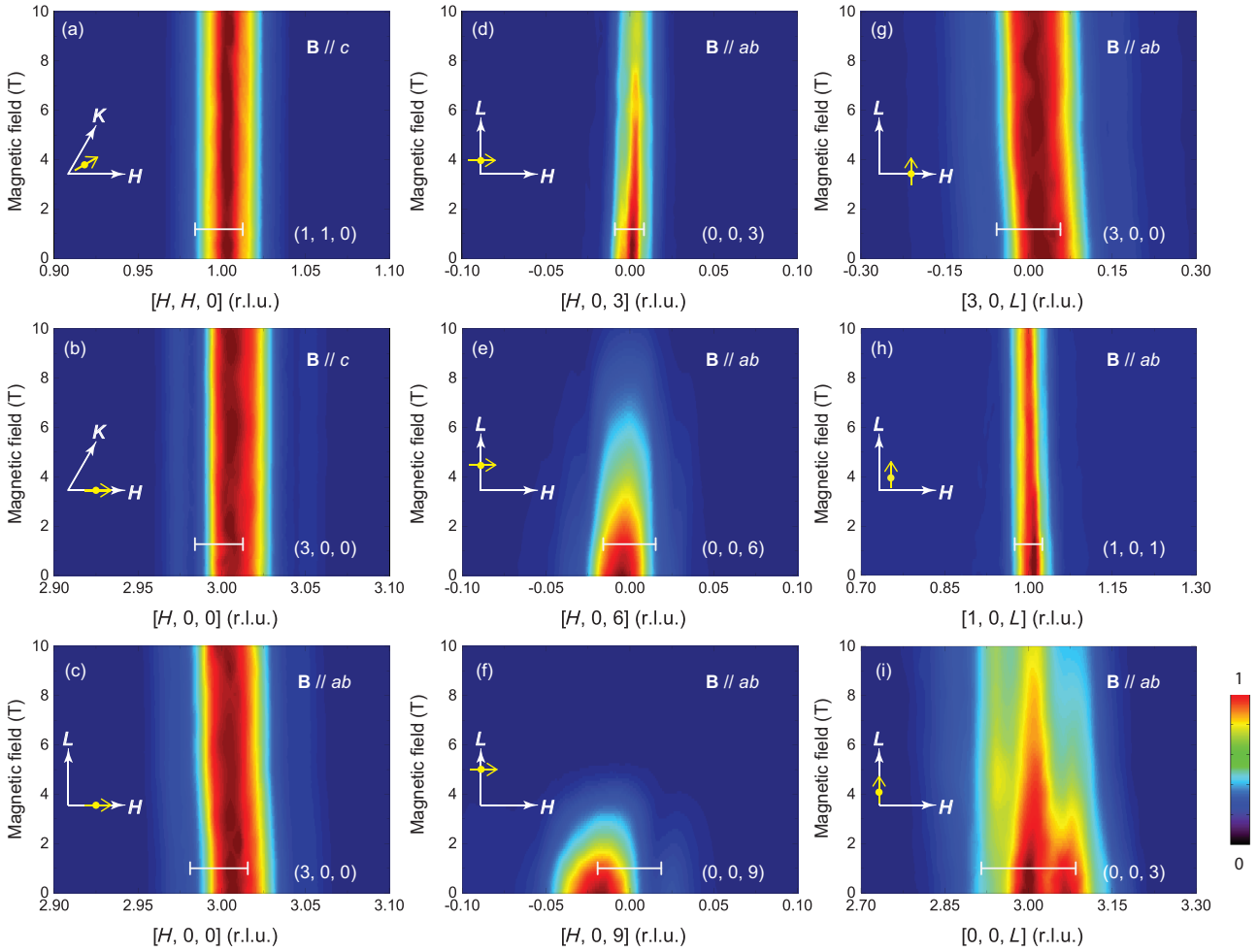

Figure 2 (Color online) Magnetic field dependence of Bragg peaks at the base temperature, T = 2 K, where the intensity was normalized by the maximum (from 0 to 1) of each peak measured at zero field. (a), (b) Magnetic field effects on the in-plane peaks at Q = (1, 1, 0) and (3, 0, 0) when **B**//c. (c)-(f) H-scans of the Bragg peaks at Q = (3, 0, 0), (0, 0, 3), (0, 0, 6), and (0, 0, 9) when **B**//ab. (g)-(i) L-scans of the Bragg peaks at Q = (3, 0, 0), (1, 0, 1), and (0, 0, 3) when **B**//ab. The horizontal bars show the full width at half maximum (FWHM) of each peak at zero field.

hibited a minimum nuclear scattering, and the magnetic scattering could be easily detected. Since the thermal triple-axis spectrometer does not feature sufficient resolution to perform the refinement of the Bragg peaks, we only focused on the total integrated intensity and changes in the center position of each peak in the magnetic field. For the H-scan at Q = (3, 0, 0) of **B**//ab, the peak center tended to shift slightly in a kink around B = 5 T, while the peak intensity was insensitive to the magnetic field (Figure 2(c)). For the peaks at Q = (0, 0, L) (L = 3, 6, 9), the magnetic field effect on the peak intensity was significant on L, as shown by the H-scans in Figure 2(d)-(f), where approximately 40% and 90% intensities of Peaks (0, 0, 3) and (0, 0, 6) were suppressed at the maximum field (B = 10 T), respectively. Surprisingly, the Bragg peak at Q = (0, 0, 9) disappeared above B = 5 T. Although the peak centers in Figure 2(d)-(f) appeared to be slightly missing alignment for the high-ordered peaks, they shifted to a high Q when the field was increased, suggesting a weak lattice distortion under magnetic field. A natural explanation for this phenomenon is thus: when the applied magnetic field tended to align the moments on Co, which were along the c-axis at the zero field, to the ab-plane, the rotation of the magnetic moments also tilted the lattice to the same direction via magnetoelastic coupling, after which such a lattice distortion shifted the high-ordered peaks from the scattering plane. To confirm this, we also performed L-scans at Q = (3, 0, 0), (1, 0, 1), and (0, 0, 3), as shown in Figure 2(g)-(i). The suppression of the intensity became more evident by increasing L from 0 to 3. A small kink also existed around B = 5 T for the L-scan of Peak (3, 0, 0), which was similar to that for the H-scan of the same peak (Figure 2(g)), thereby suggesting that the lattice was indeed distorted by the high field. The broad peak of Q = (0, 0, 3) was probably due to the multiple domains or slightly different absorptions of the neutrons during the scattering since the crystal was sufficiently large for the diffraction experiments (Figure 2(i)).

To present the magnetoelastic response of the **B**//ab geometry more clearly, we plotted the H-scans and L-scans of all

the measured Bragg peaks of $B = 0$ T and $B = 10$ T at $T = 2$ K in Figure 3, where the peak center positions from the Gaussian fittings were marked by the arrows, and the peak shift, ΔQ, was shown in each panel. For Peak (3, 0, 0) ($L = 0$), the field effect on the peak intensity was weak for the H- and L- scans, but the peak center shifted slightly. As L increased from 1, 3, and 6 to 9 (Peaks (1, 0, 1), (0, 0, 3), (0, 0, 6), to (0, 0, 9), respectively), the field effect became more significant. It appeared that the peak center shifted to the positive side of the H-scans and the low Q side of the L-scans, which could be from a distortion of the a-axis or an extension of the c-axis. Here, the small shoulders in Peak (0, 0, 9) and some dips inside Peaks (0, 0, 3) and (1, 0, 1) could be due to other small multiple domains or different absorptions of neutrons. Since most of the peaks could be well-fitted by a single Gaussian function, we employed the same method to analyze them even though the H-scans of Peak (1, 0, 1) was not exactly Gaussian-like. In the following analysis, we compared the integrated intensity with the peak center of the same peak, as such distorted peak shapes would not affect the results.

To directly compare the magnetic effect on the Bragg peaks of the two geometries, we tracked the temperature dependence of the integrated intensity and center position of the H-scans at $Q = (1, 0, 1)$ for the $\mathbf{B}//ab$ geometry and $Q = (3, 0, 0)$ and (1, 1, 0) for the $\mathbf{B}//c$ ones, and the results are shown in Figure 4. The zero-field data of Peak (1, 0, 1) revealed a kink at T_C of the ferromagnetic transition. When the in-plane field increased from 0 to 10 T, the integrated peak intensity of $Q = (1, 0, 1)$ reduced rapidly in the ferromagnetic state with approximately 25% intensity suppression at $T = 2$ K (Figure 4(a)). Moreover, the peak center also shifted to a high H side (Figure 4(b)). Although the peaks were not well-fitted by a single Gaussian function, the shift in the peak center with large error bars was consistent with the behavior of the integrated intensity. Conversely, the out-of-plane field only slightly enhanced the peak intensities at $Q = (3, 0, 0)$ and (1, 1, 0), while their peak centers were largely unchanged (Figure 4(c)-(f)). Interestingly, it appeared that the peak suppression under $\mathbf{B}//ab$ commenced at the Curie temperature, T_C, at a low field, $B = 5$ T, although it was significantly strengthened below T_A under high field, $B = 10$ T, and the enhancement of the Bragg peaks of $\mathbf{B}//c$ did not directly respond to any magnetic transitions at T_A or T_C, as determined by our transport measurements. Upon warming up from T_C to 300 K, the intensities of the two peaks decreased continuously probably because of the thermal expansion of the lattice and the weak contamination due to decreasing the quasi-elastic scattering.

To map the magnetoelastic response of $\mathbf{B}//ab$, we conducted the systematic field-dependent measurements of the H-scans at $Q = (1, 0, 1)$ from $T = 2$ to 300 K, and the results are summarized in Figure 5(a). Apparently, the peak intensity increased rapidly below T_C to generate the magnetically ordered moments, although it could be further suppressed by an external magnetic field. Apart from the critical scatterings around T_C, which persisted in all the fields, a nonmonotonic field dependence was observed between T_A and T_C. The typical field dependence of the relative peak intensity in Figure 5(b) in which the intensity appeared to recover above 6 T at $T = 149$ and 161 K implied a complex magnetoelastic coupling in this region.

4 Discussion

The slight enhancement of the Bragg peak intensity of $\mathbf{B}//c$

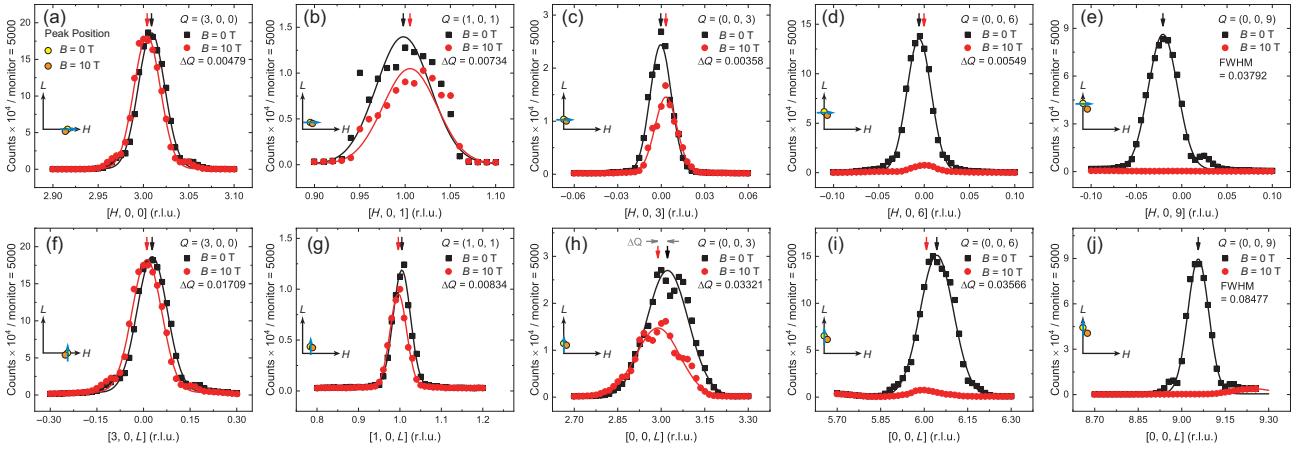

Figure 3 (Color online) Comparison of the Bragg peaks of $B = 0$ and 10 T at $T = 2$ K and $\mathbf{B}//ab$. (a)-(e) H-scans of the Bragg peaks at $Q = (3, 0, 0)$, (1, 0, 1), (0, 0, 3), (0, 0, 6), and (0, 0, 9). (f)-(j) L-scans of the Bragg peaks at $Q = (3, 0, 0)$, (1, 0, 1), (0, 0, 3), (0, 0, 6), and (0, 0, 9). The arrows indicate the peak center positions obtained from the Gaussian fittings, and the shifts of peak centers, ΔQ, are presented in each panel. FWHM of Peak (0, 0, 9) is shown in (e) and (j).

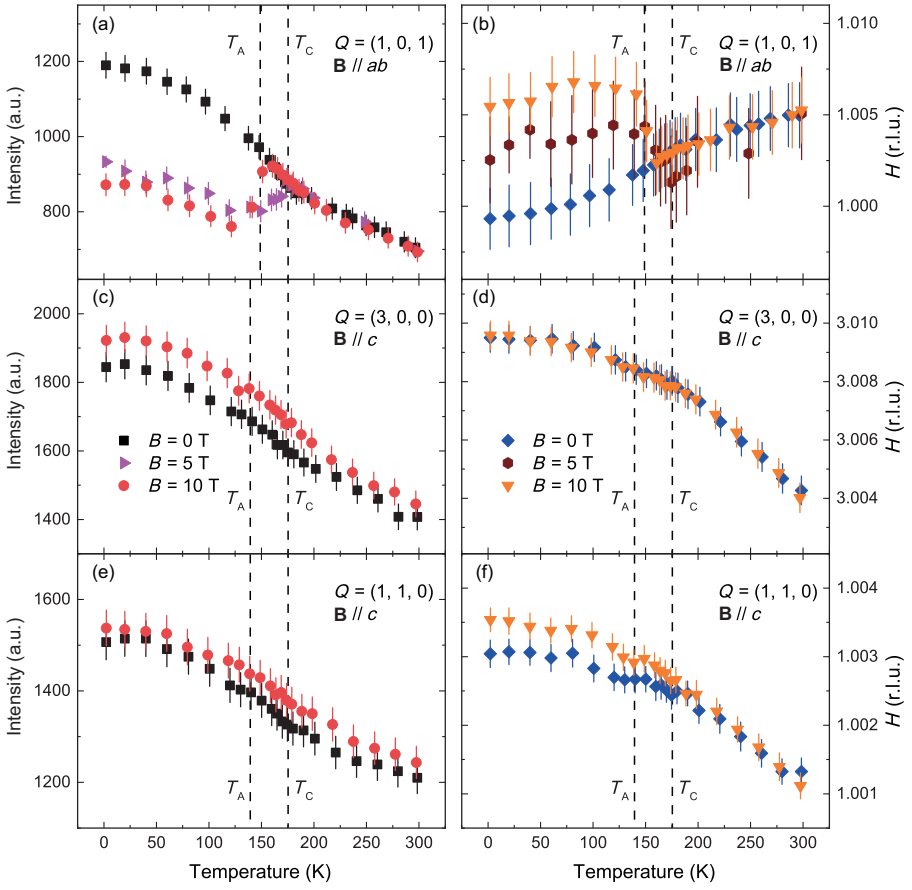

Figure 4 (Color online) Temperature dependence of the field effect on the integrated intensity and center position of the Bragg peaks. (a), (b) Field effect on the Bragg peak at $Q = (1, 0, 1)$ when the **B**//*ab* geometry was measured by the FC method. (c), (d) Field effect on the Bragg peak at $Q = (3, 0, 0)$ when the **B**//*c* geometry was measured by the ZFC method. (e), (f) Field effect on the Bragg peak at $Q = (1, 1, 0)$ when the **B**//*c* geometry was measured by the ZFC method. The error bars are from the single Gaussian fitting of the Bragg peaks. Notably, here T_A is different in the two cases, as shown by Figure 1(e).

could be easily understood as the polarization effects on the ferromagnetic domains, which already existed above T_C, in the zero field and turn to align along the magnetic field. Previous results suggested that the T_C might increase up to 200 K at $B = 6$ T for the **B**//*c* geometry [31], and this is consistent with the intensity enhancement in our results (Figure 4(c) and (e)), where the in-plane magnetic order was rapidly suppressed within $B = 0.1$ T.

The suppression of the Bragg peak intensity of **B**//*ab*, which was accompanied by a distortion of the lattice, indicated very strong magnetoelastic coupling in the magnetic state. In the $Co_3Sn_2S_2$ compound, T_A is considered to be related to an in-plane antiferromagnetic order [31], although it depended on the sample quality and probing methods. When approaching T_C from a low temperature, the magnetic moments of Co atoms might tilt slightly toward the center of the kagome lattice and lose the long-range correlations [14]. This effect would generate frustrated in-plane magnetic components in the kagome lattice, which would cause a complicated transition around T_A. Since the *c*-axis polarized ferromagnetism was not well-developed above T_A to compete with the in-plane antiferromagnetic order, the in-plane magnetoelastic response become stronger below T_A. Between T_A and T_C, the in-plane field interacted with both the in-plane and out-of-plane magnetic orders and tended to align the moments toward the field direction. Thus, the frustration of the in-plane order might be enhanced to exhibit the nonmonotonic behaviors of the measured peak intensity between T_A and T_C.

However, the probability that the sample was pulled off the Al plate by a strong magnetic torque during our measurements must be carefully eliminated. Considering that the saturation moment is weak (0.3 μ_B/Co) [22, 23], the magnetic torque on our sample with a maximum in-plane field, $B = 10$ T, was not adequately to pull the well-mounted sample or cause the plastic deformation of the sample holder, which would cause irreversible displacements in the sample orientation. For the ZFC measurements, the sample magnetization would be a multi-domain, and the macroscopic torque would be very small. In fact, after several cycles of the temperature and field changes, the measured Bragg peaks were very reproducible through *Q*-scans under the same conditions re-

gardless of the sequence of the changing field or temperature. Therefore, the peak suppression was more likely induced by the magnetoelastic response rather than the magnetic torque interaction.

Although the probability of small elastic bending in the Al sample holder due to the magnetic torque, which is reversible in the magnetic field, must be considered, it should present a linear response to the peak intensity rather than to the nonlinear behaviors, as shown in Figure 5. Thus, the actual magnetoelastic response of $\mathbf{B}//ab$ might be weaker than what we observed. Specifically, the tilt of the whole crystal due to the bending of the holder would only induce a rigid shift in the wavevector (Q) from the scattering plane, although the lattice distortion exerted an additional effect on the Q value. Since the peak centers shifted in the magnetic field and the peak intensities at (0, 0, L) (L = 3, 6, 9) disappeared in very different fields, we believe that it was largely induced by the lattice distortion, which exerted a more significant effect than the elastic bending of the plate. Further, we quantitatively estimated and compared the effects of the internal lattice distortion and the tilting of the external sample holder with the mosaic of the samples. From the results, which are shown in Figure 3, we listed the peak center shifts (ΔQ) between B = 0 T and B = 10 T in Table 1 for the H-scans of Peak (3, 0, 0) and the L-scans of Peaks (1, 0, 1), (0, 0, 3), (0, 0, 6), and (0, 0, 9). Regarding Peak (0, 0, 9), as the peak intensities disappeared at 10 T, the shift should be larger than FWHM, which was approximately ΔQ = 0.0848 (r.l.u.). For a rigid shift, we only measured the tails of those Bragg peaks within the mosaic of the sample at $q = Q\cos\theta$, as follows: $\Delta Q = Q(1-\cos\theta)$, where $Q = H$ (or L) in reciprocal lattice unit (r.l.u.) of Q_H (or Q_L). Apparently, the external tilt angle, which was presented in Table 1, is much larger than that of the mosaic ($\sim 1°$), and this could cause the disappearance of all the peaks in the fixed scattering plane and not only Peak (0, 0, 9). Alternatively, we considered an additional distortion of the lattice by assuming the c-axis was slightly extended by the magnetoelastic coupling effect, thereby shrinking Q_L. In this case, we obtained the following: $\Delta Q = Q - Q'\cos\theta'$, where $Q \neq Q'$. For example, consider a small lattice distortion of $Q'_L = 0.9942Q_L$, the tilt angles of the c-axis would be much smaller, even as small as 1°, thus making the peaks detectable at low Ls. Similarly, the peak shift of (3, 0, 0) requires approximately 3.2° in the rigid tilting case, which is much larger than that of the in-plane mosaic (~0.8°). In such a case, Peak (3, 0, 0) would be strongly affected or might completely disappear, and this was definitely not the case in our experiment. By assuming a very small change in the a-axis (approximately 0.16%), such a peak shift and nearly unchanged intensity is possible. Besides, Peak (3, 0, 0) accounted for very weak contribution to the magnetic scattering at L = 0 plane. Thus, the magnetoelastic effect on this peak is expected to be weaker than on other peaks. Notably, the calculated tilting angles were not very consistent if only one case was to be considered in Table 1. More likely, both the small elastic tilting of the sample holder and the lattice distortion co-existed in the high magnetic field. Furthermore, there might be symmetry breaking of the lattice structure in the magnetic field, which may cause significant changes in the peak intensity, even within the scattering plane. However, since we applied the triple-axis mode for the measurements, the Lorentz factor was also sensitive to the scattering angle, and the peak shape and intensity were not adequately defined. Since we could not achieve full refinement by the limited data from our triple-axis experiments, further comprehensive studies utilizing a single-

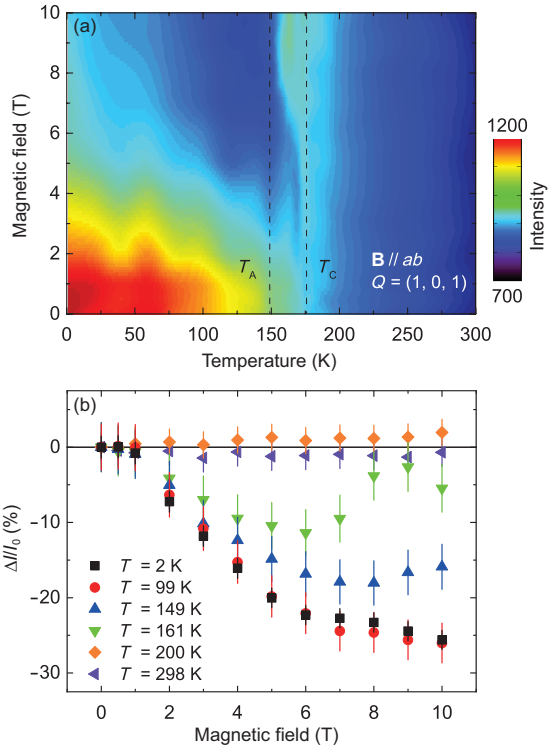

Figure 5 (Color online) (a) Temperature and field dependence on the integrated intensity of the Bragg peak at Q = (1, 0, 1) when $\mathbf{B}//ab$. The data were measured by loop-setting the field at different temperatures. The temperature steps were the same as those shown in Figure 4(a) and (b). (b) Field dependence of the relative peak intensity ($\Delta I/I_0 = (I_B - I_0)/I_0$) at typical temperatures (T = 2, 99, 149, 161, 200, and 298 K).

Table 1 Estimation of the shift of the peak center under external tile and internal distortion

Bragg Peak	Center shift ΔQ (r.l.u.)	External tilt θ (°)	Internal distortion θ' (°)
$(3, 0, 0)_H$	0.00479	3.2	/
$(1, 0, 1)_L$	0.00834	7.4	4.1
$(0, 0, 3)_L$	0.03321	8.5	5.9
$(0, 0, 6)_L$	0.03566	6.2	1.0
$(0, 0, 9)_L$	0.08477	7.9	4.9

crystal neutron diffractometer in a magnetic field are highly desired to clarify this shortcoming.

Finally, we also noticed that the negative orbital magnetism in **B**//c was inconsistent with our results [32] (the suppression of the Bragg peak in our work only occurred in **B**//ab because of the magnetoelastic coupling). However, by assuming a small in-plane component of the magnetic field from a possible deviation between the c-axis and **B**, suppression of the magnetism would be achieved whether **B** is positive or negative. Accordingly, any measurement of $Co_3Sn_2S_2$ in the magnetic field should carefully consider the anisotopic magnetoelastic response, as demonstrated in our results. From our previous magnetization measurements, the in-plane saturation field was approximately 23 T at T = 2 K, which is significantly different from the out-of-plane saturation field (about 0.09 T) [35], thus suggesting large magnetocrystalline anisotropy with a coefficient, K_u, of up to 8.3×10^5 J m^{-3}. Although it is difficult to fully align the small magnetic moment on the Co kagome lattice from the c-axis to the ab-plane, the in-plane field of up to 10 T in our experiments is sufficient to cause a lattice distortion under such strong coupling. Therefore, the in-plane magnetic field, (**B**//ab), is more efficient than the out-of-plane magnetic field, (**B**//c), for tuning the lattice in $Co_3Sn_2S_2$ via the magnetoelastic coupling.

Interestingly, SOC is generally crucial in quasi-2D ferromagnets. Thus, both the magnetism and lattice could be affected by a magnetic field. For example, the SOC-induced magnetic anisotropy stabilized the ferromagnetic order in the 2D van der Waals material, CrI_3 [39, 40], and a magnetic field induced a transition from the 2D kagome state to a 3D long-range ferromagnetic order in $Yb_2Ti_2O_7$ [41]. Particularly, in a recently investigated kagome ferromagnet, Fe_3Sn_2, which possessed massive Dirac fermions in its topological bands [42], the textures of the magnetic domain and spin orientations were highly sensitive to the in-plane magnetic field [43, 44]. Although the in-plane resistivity of $Co_3Sn_2S_2$ exhibited a small response to the lattice distortion that was mostly related to the c-axis, as shown in Figure 1(f), other transport properties, such as AHC, Nernst signals, and the in-plane magnetoresistance, would be probably affected greatly by canting the magnetization from the easy axis [35, 45]. Hence, the topological states of $Co_3Sn_2S_2$ could be tuned by applying magnetic fields.

5 Conclusions

To summarize, the effects of a magnetic field on magnetism and the lattice of a newly discovered Weyl semimetal, $Co_3Sn_2S_2$, were studied via elastic neutron scattering. Although the Bragg peaks were only slightly enhanced by the out-of-plane field (**B**//c), they were significantly affected by the in-plane field (**B**//ab) with a suppression of the intensity and lattice distortion below T_A probably by strong magnetoelastic coupling. A nonmonotonic behavior of the peak intensity in the field between T_A and T_C was observed and attributed to the competing magnetic phases. Such anisotropic magnetoelastic response and its strong field and temperature dependence afforded us new opportunities for tuning the magnetism and lattice, as well as the topological states of this fascinating material.

This work was supported by the National Key Research and Development Program of China (Grant Nos. 2017YFA0303100, 2017YFA0302900, 2016YFA0300500, and 2017YFA0206300), the National Natural Science Foundation of China (Grant Nos. 11974392, 11974394, 11822411, 51722106, 11674372, 11774399, 11961160699, and 12061130200), the Strategic Priority Research Program (B) of the Chinese Academy of Sciences (CAS) (Grant Nos. XDB07020300, XDB25000000, and XDB33000000), and the Beijing Natural Science Foundation (Grant Nos. JQ19002, Z180008, and Z190009). EnKe Liu and HuiQian Luo is grateful for the support from the Youth Innovation Promotion Association of Chinese Academy of Sciences (Grant Nos. 2013002, and 2016004). This work is based on neutron scattering experiments performed at the Swiss Spallation Neutron Source (SINQ), Paul Scherrer Institute, Villigen, Switzerland (Proposal No. 20181447).

1 Z. Fang, N. Nagaosa, K. S. Takahashi, A. Asamitsu, R. Mathieu, T. Ogasawara, H. Yamada, M. Kawasaki, Y. Tokura, and K. Terakura, Science **302**, 92 (2003), arXiv: cond-mat/0310232.
2 N. Nagaosa, J. Sinova, S. Onoda, A. H. MacDonald, and N. P. Ong, Rev. Mod. Phys. **82**, 1539 (2010), arXiv: 0904.4154.
3 A. A. Zyuzin, S. Wu, and A. A. Burkov, Phys. Rev. B **85**, 165110 (2012), arXiv: 1201.3624.
4 H. Weng, R. Yu, X. Hu, X. Dai, and Z. Fang, Adv. Phys. **64**, 227 (2015), arXiv: 1508.02967.
5 C. X. Liu, S. C. Zhang, and X. L. Qi, Annu. Rev. Condens. Matter Phys. **7**, 301 (2016).
6 B. Yan, and C. Felser, Annu. Rev. Condens. Matter Phys. **8**, 337 (2017), arXiv: 1611.04182.
7 K. Manna, Y. Sun, L. Muechler, J. Kübler, and C. Felser, Nat. Rev. Mater. **3**, 244 (2018), arXiv: 1802.03771.
8 J. Zou, Z. He, and G. Xu, npj Comput. Mater. **5**, 96 (2019), arXiv: 1909.11999.
9 H. Weng, C. Fang, Z. Fang, B. A. Bernevig, and X. Dai, Phys. Rev. X **5**, 011029 (2015), arXiv: 1501.00060.
10 F. D. M. Haldane, Phys. Rev. Lett. **93**, 206602 (2004), arXiv: cond-mat/0408417.
11 G. Xu, H. Weng, Z. Wang, X. Dai, and Z. Fang, Phys. Rev. Lett. **107**, 186806 (2011), arXiv: 1106.3125.
12 A. A. Burkov, Phys. Rev. Lett. **113**, 187202 (2014), arXiv: 1406.3033.
13 R. Karplus, and J. M. Luttinger, Phys. Rev. **95**, 1154 (1954).
14 E. Liu, Y. Sun, N. Kumar, L. Muechler, A. Sun, L. Jiao, S. Y. Yang, D. Liu, A. Liang, Q. Xu, J. Kroder, V. Süß, H. Borrmann, C. Shekhar, Z. Wang, C. Xi, W. Wang, W. Schnelle, S. Wirth, Y. Chen, S. T. B. Goennenwein, and C. Felser, Nat. Phys. **14**, 1125 (2018), arXiv: 1712.06722.
15 Q. Wang, Y. Xu, R. Lou, Z. Liu, M. Li, Y. Huang, D. Shen, H. Weng, S. Wang, and H. Lei, Nat. Commun. **9**, 3681 (2018), arXiv: 1712.09947.
16 H. M. Weng, Sci. China-Phys. Mech. Astron. **62**, 127031 (2019).
17 R. Weihrich, I. Anusca, and M. Zabel, Z. Anorg. Allg. Chem. **631**, 1463 (2005).
18 R. Weihrich, and I. Anusca, Z. Anorg. Allg. Chem. **632**, 1531 (2006).

19 M. A. Kassem, Y. Tabata, T. Waki, and H. Nakamura, J. Cryst. Growth **426**, 208 (2015).
20 M. A. Kassem, Y. Tabata, T. Waki, and H. Nakamura, J. Solid State Chem. **233**, 8 (2016).
21 Y. S. Dedkov, M. Holder, S. L. Molodtsov, and H. Rosner, J. Phys.-Conf. Ser. **100**, 072011 (2008).
22 W. Schnelle, A. Leithe-Jasper, H. Rosner, F. M. Schappacher, R. Pöttgen, F. Pielnhofer, and R. Weihrich, Phys. Rev. B **88**, 144404 (2013).
23 P. Vaqueiro, and G. G. Sobany, Solid State Sci. **11**, 513 (2009).
24 M. A. Kassem, Y. Tabata, T. Waki, and H. Nakamura, J. Phys. Soc. Jpn. **85**, 064706 (2016).
25 Q. Xu, E. Liu, W. Shi, L. Muechler, J. Gayles, C. Felser, and Y. Sun, Phys. Rev. B **97**, 235416 (2018), arXiv: 1801.00136.
26 D. F. Liu, A. J. Liang, E. K. Liu, Q. N. Xu, Y. W. Li, C. Chen, D. Pei, W. J. Shi, S. K. Mo, P. Dudin, T. Kim, C. Cacho, G. Li, Y. Sun, L. X. Yang, Z. K. Liu, S. S. P. Parkin, C. Felser, and Y. L. Chen, Science **365**, 1282 (2019), arXiv: 1909.09580.
27 N. Morali, R. Batabyal, P. K. Nag, E. Liu, Q. Xu, Y. Sun, B. Yan, C. Felser, N. Avraham, and H. Beidenkopf, Science **365**, 1286 (2019), arXiv: 1903.00509.
28 R. Yang, T. Zhang, L. Zhou, Y. Dai, Z. Liao, H. Weng, and X. Qiu, Phys. Rev. Lett. **124**, 077403 (2020), arXiv: 1908.03895.
29 Y. Xu, J. Zhao, C. Yi, Q. Wang, Q. Yin, Y. Wang, X. Hu, L. Wang, E. Liu, G. Xu, L. Lu, A. A. Soluyanov, H. Lei, Y. Shi, J. Luo, and Z. G. Chen, Nat. Commun. **11**, 3985 (2020), arXiv: 1908.04561.
30 M. A. Kassem, Y. Tabata, T. Waki, and H. Nakamura, Phys. Rev. B **96**, 014429 (2017), arXiv: 1702.05627.
31 Z. Guguchia, J. A. T. Verezhak, D. J. Gawryluk, S. S. Tsirkin, J. X. Yin, I. Belopolski, H. Zhou, G. Simutis, S. S. Zhang, T. A. Cochran, G. Chang, E. Pomjakushina, L. Keller, Z. Skrzeczkowska, Q. Wang, H. C. Lei, R. Khasanov, A. Amato, S. Jia, T. Neupert, H. Luetkens, and M. Z. Hasan, Nat. Commun. **11**, 559 (2020).
32 J. X. Yin, S. S. Zhang, G. Chang, Q. Wang, S. S. Tsirkin, Z. Guguchia, B. Lian, H. Zhou, K. Jiang, I. Belopolski, N. Shumiya, D. Multer, M. Litskevich, T. A. Cochran, H. Lin, Z. Wang, T. Neupert, S. Jia, H. Lei, and M. Z. Hasan, Nat. Phys. **15**, 443 (2019), arXiv: 1901.04822.
33 J. X. Yin, N. Shumiya, Y. Jiang, H. Zhou, G. Macam, S. S. Zhang, H. O. M. Sura, Z. Cheng, Z. Guguchia, Y. Li, Q. Wang, M. Litskevich, I. Belopolski, X. Yang, T. A. Cochran, G. Chang, Q. Zhang, B. M. Andersen, Z. Q. Huang, F. C. Chuang, H. Lin, H. Lei, Z. Wang, S. Jia, and M. Z. Hasan, arXiv: 2002.11783.
34 Y. Xing, J. Shen, H. Chen, L. Huang, Y. Gao, Q. Zheng, Y. Y. Zhang, G. Li, B. Hu, G. Qian, L. Cao, X. Zhang, P. Fan, R. Ma, Q. Wang, Q. Yin, H. Lei, W. Ji, S. Du, H. Yang, W. Wang, C. Shen, X. Lin, E. Liu, B. Shen, Z. Wang, and H. J. Gao, Nat. Commun. **11**, 5613 (2020), arXiv: 2001.11295.
35 J. Shen, Q. Zeng, S. Zhang, W. Tong, L. Ling, C. Xi, Z. Wang, E. Liu, W. Wang, G. Wu, and B. Shen, Appl. Phys. Lett. **115**, 212403 (2019), arXiv: 2002.03940.
36 C. Liu, J. L. Shen, J. C. Gao, C. J. Yi, D. Liu, T. Xie, L. Yang, S. Danilkin, G. C. Deng, W. H. Wang, S. L. Li, Y. G. Shi, H. M. Weng, E. K. Liu, and H. Q. Luo, Sci. China-Phys. Mech. Astron. **64**, 217062 (2021), arXiv: 2006.07339.
37 X. C. Xie, Sci. China-Phys. Mech. Astron. **64**, 217061 (2021).
38 B. H. Yan, Sci. China-Phys. Mech. Astron. **64**, 217063 (2021).
39 L. Chen, J. H. Chung, B. Gao, T. Chen, M. B. Stone, A. I. Kolesnikov, Q. Huang, and P. Dai, Phys. Rev. X **8**, 041028 (2018), arXiv: 1807.11452.
40 L. Chen, J. H. Chung, T. Chen, C. Duan, A. Schneidewind, I. Radelytskyi, D. J. Voneshen, R. A. Ewings, M. B. Stone, A. I. Kolesnikov, B. Winn, S. Chi, R. A. Mole, D. H. Yu, B. Gao, and P. Dai, Phys. Rev. B **101**, 134418 (2020).
41 K. A. Ross, J. P. C. Ruff, C. P. Adams, J. S. Gardner, H. A. Dabkowska, Y. Qiu, J. R. D. Copley, and B. D. Gaulin, Phys. Rev. Lett. **103**, 227202 (2009), arXiv: 0902.0329.
42 L. Ye, M. Kang, J. Liu, F. von Cube, C. R. Wicker, T. Suzuki, C. Jozwiak, A. Bostwick, E. Rotenberg, D. C. Bell, L. Fu, R. Comin, and J. G. Checkelsky, Nature **555**, 638 (2018), arXiv: 1709.10007.
43 Y. Li, Q. Wang, L. DeBeer-Schmitt, Z. Guguchia, R. D. Desautels, J. X. Yin, Q. Du, W. Ren, X. Zhao, Z. Zhang, I. A. Zaliznyak, C. Petrovic, W. Yin, M. Z. Hasan, H. Lei, and J. M. Tranquada, Phys. Rev. Lett. **123**, 196604 (2019), arXiv: 1907.04948.
44 N. Kumar, Y. Soh, Y. Wang, and Y. Xiong, Phys. Rev. B **100**, 214420 (2019), arXiv: 1908.03927.
45 M. P. Ghimire, J. I. Facio, J. S. You, L. Ye, J. G. Checkelsky, S. Fang, E. Kaxiras, M. Richter, and J. van den Brink, Phys. Rev. Res. **1**, 032044 (R) (2019).